Pulling Order Back from the Brink of Disorder: Observation of a Nodal-Line Spin Liquid and Fluctuation Stabilized Order in K_2IrCl_6

Qiaochu Wang,[1] Alberto de la Torre,[1,*] Jose A. Rodriguez-Rivera,[2,3] Andrey A. Podlesnyak,[4] Wei Tian,[4] Adam A. Aczel,[4] Masaaki Matsuda,[4] Philip J. Ryan,[5] Jong-Woo Kim,[5] Jeffrey G. Rau,[6] and Kemp W. Plumb[1,†]

[1]*Department of Physics, Brown University, Providence, Rhode Island 02912, USA*
[2]*NIST Center for Neutron Research, National Institute of Standards and Technology, Gaithersburg, Maryland 20899, USA*
[3]*Department of Materials Science and Engineering, University of Maryland, College Park, Maryland 20742, USA*
[4]*Neutron Scattering Division, Oak Ridge National Laboratory, Oak Ridge, Tennessee 37831, USA*
[5]*X-ray Science Division, Argonne National Laboratory, Argonne, Illinois 60439, USA*
[6]*Department of Physics, University of Windsor, Windsor, Ontario, N9B 3P4, Canada*

(Received 22 July 2024; revised 23 November 2024; accepted 14 January 2025; published 21 April 2025)

Competing interactions in frustrated magnets can give rise to highly degenerate ground states from which correlated liquidlike states of matter often emerge. The scaling of this degeneracy influences the ultimate ground state, with extensive degeneracies potentially yielding quantum spin liquids, while subextensive or smaller degeneracies yield static orders. A long-standing problem is to understand how ordered states precipitate from this degenerate manifold and what echoes of the degeneracy survive ordering. Here, we use neutron scattering to experimentally demonstrate a new "nodal-line" spin liquid, where spins collectively fluctuate within a subextensive manifold spanning one-dimensional lines in reciprocal space. Realized in the spin-orbit-coupled, face-centered-cubic iridate K_2IrCl_6, we show that the subextensive degeneracy is robust, but remains susceptible to fluctuations or longer-range interactions which cooperate to select a magnetic order at low temperatures. Proximity to the nodal-line spin liquid influences the ordered state, enhancing the effects of quantum fluctuations that in turn act to stabilize the sublattice magnetization through the self-consistent opening of a large spin-wave gap. Our results demonstrate how quantum fluctuations can act counterintuitively in frustrated materials: Even in a case where fluctuations are ineffective at selecting an ordered state from a degenerate manifold, at the brink of the nodal spin liquid, they can act to protect the ordered state and dictate its low-energy physics.

DOI: 10.1103/PhysRevX.15.021021 Subject Areas: Condensed Matter Physics, Magnetism

I. INTRODUCTION

The promise of discovering novel states of matter governed by quantum and thermal fluctuations drives a sustained interest in highly frustrated magnetic materials. One of the oldest and most important examples is the Heisenberg antiferromagnet (AFM) on the face-centered-cubic (fcc) lattice. Anderson [1] showed that classically its ground-state degeneracy scales subextensively in the system size and includes coplanar spin spirals characterized by all magnetic wave vectors spanning one-dimensional lines in reciprocal space. As the temperature is lowered, fluctuations of the spins become more confined to states on these lines, forming a correlated state we term a "nodal-line spin liquid." This spin liquid is distinguished from a conventional paramagnet by having growing correlations along two spatial directions as the temperature is lowered but only short-range correlations along the third. As shown in Fig. 1, some examples of correlated paramagnets include spiral-spin liquids, where the degenerate states span surfaces in momentum space [2,3], and classical spin liquids [4–8], where degenerate states span a volume, and all exhibit significant and structured magnetic correlations. Among these correlated paramagnets, the nodal-line spin liquid has the least degeneracy and thus sits closest to conventional magnetic order.

Because of its subextensive degeneracy, the nodal-line spin liquid is susceptible to order via quantum or thermal fluctuations—"order by disorder" [9–12]. For the fcc

*Present address: Department of Physics, Northeastern University, Boston, Massachusetts 02115, USA.
†Contact author: kemp_plumb@brown.edu

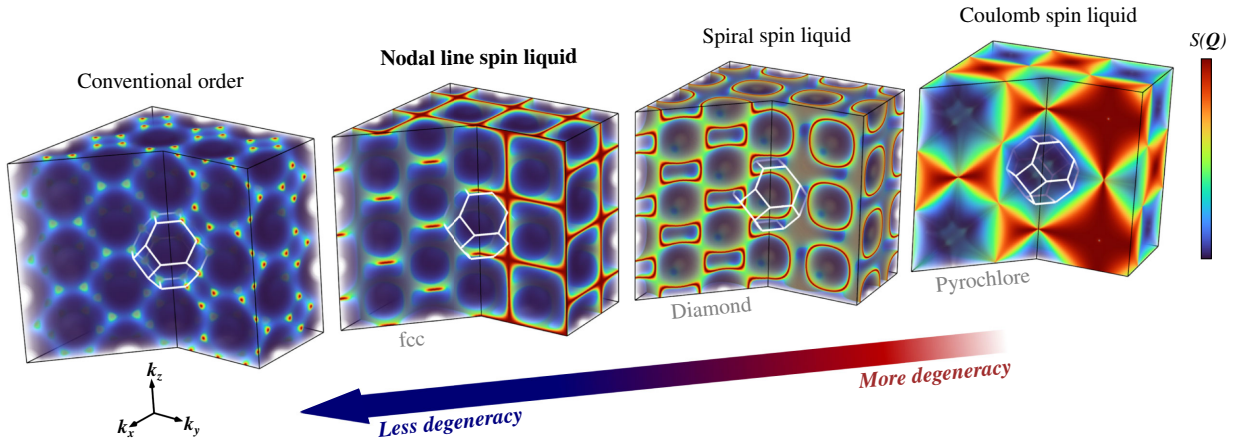

FIG. 1. Illustration of the spin correlations encoded in the equal time structure factors $S(\boldsymbol{Q})$ of a variety of model magnetic phases: from the highly frustrated extensively degenerate Coulomb spin liquid and subextensively degenerate spiral and nodal spin liquids to conventional magnetic order. These structured correlations are present throughout momentum space for the Coulomb case, along surfaces for the spiral-spin liquid, along lines for the nodal-line spin liquid, and are confined to points for conventional order.

Heisenberg AFM, thermal [13,14] and quantum [15] fluctuations each favor a subextensive set of collinear Néel states [1,16], both ultimately selecting so-called "type-I" magnetic order characterized by a (1, 0, 0) propagation vector [Fig. 2(a)]. However, the selection of this type-I order among the collinear states is extremely weak, with an energy difference of only approximately 0.25% of the Heisenberg exchange J, and with many other metastable collinear states lying within approximately 1% of J in energy [15]. While the classical degeneracy of the nodal-line spin liquid and fluctuation-induced selection are robust to nearest-neighbor anisotropic exchange interactions, it can be lifted energetically by further-neighbor couplings. For example, next-nearest-neighbor (NNN) Heisenberg exchange selects type-I order when ferromagnetic, but selects the "type-III" state, a collinear Néel order with propagation vector (1, 0.5, 0) [Fig. 2(b)], when antiferromagnetic [17].

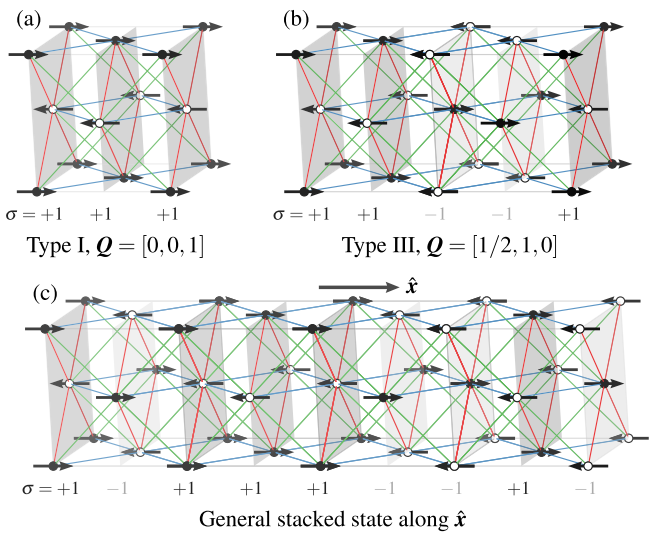

FIG. 2. Illustration of several magnetic ground states of the Heisenberg-Kitaev-Γ model on the fcc lattice when $K > 0$, including (a) type-I and (b) type-III Néel states and (c) and example of a generic "stacked" state formed by Néel planes stacked along the $\hat{\boldsymbol{x}}$ direction. Moments are parallel or antiparallel to the stacking direction, with the stacked Néel planes highlighted, and all magnetic ordering vectors $\boldsymbol{Q}$ are indexed in the cubic fcc unit cell.

In each case, ordering out of the nodal-line spin liquid proceeds through a multistep process. First, order by disorder singles out the submanifold of discrete collinear states from the continuous manifold of the nodal-line spin liquid. Despite their near degeneracy, each of these local minima exhibits conventional magnetic order with no gapless spin-wave excitations, aside from any required Goldstone modes. Second, a specific collinear state among the local minima is selected by either fluctuations or energetic effects. While the ordered state is ultimately determined by the second stage, the low-energy physics—including the excitations and thermodynamic properties—are dictated by the fluctuation-induced selection arising in the first stage. This leads to a counterintuitive result: Even though the final order-by-disorder selection of the ground state is very weak, each of the collinear states is stable, with a large spin-wave gap generated by strong quantum fluctuations along the nodal-line directions of the parent spin liquid. This large gap then suppresses fluctuations that would otherwise reduce the ordered moment. Thus, despite the difficulty of fluctuations in selecting a unique ground state, they act to stabilize whichever particular ordering is singled out by subleading perturbations and ultimately dictate the physics of the material.

While much theoretical and experimental effort has been made on fcc AFMs [18–25], a clear example of this physics has not been found. An important compound in this context is the vacancy-ordered double perovskite K_2IrCl_6 which has sustained more than 70 years of interest [18–22,26–38].

Despite such an effort, the magnetic Hamiltonian of K_2IrCl_6 has yet to be resolved due to an absence of any inelastic neutron-scattering data. In addition to the presence of geometric frustration, the magnetic degrees of freedom in K_2IrCl_6 are spin-orbital entangled $j = 1/2$ states [39] supporting bond-dependent Kitaev interactions, which are believed to be significant relative to the Heisenberg exchange [24,28,36,40]. A minimal nearest-neighbor Hamiltonian including Kitaev exchange can be written [41]

$$\sum_{\langle ij\rangle_\gamma}\left[JS_i\cdot S_j + KS_i^\gamma S_j^\gamma\right], \tag{1}$$

where we have divided the bonds of the lattice into three types: x, y, and z, depending on whether they lie in the cubic yz, zx, or xy planes. Early magnetic neutron-diffraction experiments on K_2IrCl_6 revealed a type-III antiferromagnetic order below approximately 3 K [31] shown in Fig. 2(b). Based on this observation and a consistent explanation of the bulk magnetic properties, K_2IrCl_6 has long been considered to represent a near ideal fcc lattice with weak antiferromagnetic NNN interactions [36,37]. However, recent electron spin resonance measurements indicate NNN terms may play only a perturbative role and order-by-disorder physics may be essential [38] in explaining its properties. To date, there are no reported measurements of momentum-resolved dynamic correlations characterizing the excitation spectrum of this highly frustrated anisotropic magnet.

In this article, we show the physics of this nodal-line spin liquid, and its consequences in the ordered phase is realized in K_2IrCl_6. First, through comprehensive neutron-scattering measurements and theoretical modeling of the dynamic spin correlations, we conclusively demonstrate that K_2IrCl_6 is a nearly ideal realization of the Heisenberg-Kitaev model on the fcc lattice. This model is highly frustrated, with a specific Néel ordering only weakly selected by small NNN interactions or by quantum fluctuations even in the presence of Kitaev interactions. Despite the appearance of static magnetic order, as observed by diffraction measurements, a hard excitation gap, and long-lived spin waves, linear spin-wave theory (LSWT) theory completely fails as a description of magnetic excitations in K_2IrCl_6. Instead, we find that the physics of the excitation spectrum is dominated by fluctuation effects that generate a large, approximately 0.7 meV, excitation gap—about 30% of the overall approximately 2.5-meV magnon bandwidth. Above the Néel temperature $T_N = 3.1$ K, we establish that the nodal-line spin liquid survives as a thermally stable phase, even in the presence of significant Kitaev interactions that act to lower the symmetry from continuous to discrete. We demonstrate that the magnetic correlations in this phase form characteristic one-dimensional rods in reciprocal space, as illustrated in Fig. 1. The proximity to the nodal-line spin liquid in this Heisenberg-Kitaev magnet enhances quantum fluctuations that open the self-consistent gap and, counterintuitively, act to stabilize the sublattice magnetization in the ordered phase by quenching out the zero-point corrections to the ordered moment.

II. FLUCTUATION-INDUCED SPIN-WAVE GAP

We first present inelastic neutron-scattering spectra collected at $T = 300$ mK, well below the onset of type-III (0.5, 0, 1) magnetic order shown in Fig. 3. There are sharp spin waves present throughout the Brillouin zone spanning a bandwidth of 2.5 meV with a (0.7 ± 0.05)-meV gap at the (1, 0, 0) dispersion minimum. Although the strong neutron absorption from Ir places limitations on the signal-to-noise ratio and achievable energy resolution of our experiments, the spectrum we observe is dominated by resolution-limited single-magnon excitations, and any multimagnon scattering is not measurable. The observed spectrum is surprising for two reasons. First, the dispersion minimum does not occur at the wave vector of static magnetic order (1, 0.5, 0), but instead near (1, 0, 0), and second for the generic symmetry-allowed spin model relevant to K_2IrCl_6, LSWT predicts a gapless pseudo-Goldstone mode in the type-III phase [42,43].

The large excitation gap could potentially be explained within LSWT by a reduction of the crystal symmetry from cubic to (say) tetragonal, as might arise from a weak structural distortion at T_N [24,44] or may arise self-consistently from quantum fluctuations. Given the documented structural instabilities in the vacancy-ordered double perovskites [35–37], we first rule out lattice distortions as the origin of the excitation gap. We then consider the effects of quantum fluctuations through nonlinear spin-wave theory (NLSWT) for the fcc Heisenberg-Kitaev model and show that such quantum fluctuations are responsible for the large spin-wave gap in K_2IrCl_6.

A. Ruling out a lattice distortion as the origin of the gap

Although all previous diffraction measurements have reported K_2IrCl_6 as cubic for $T < T_N$ [36,37], there is spectroscopic evidence that K_2IrCl_6 may exhibit local structural distortions [45]. Furthermore, recent high-resolution single-crystal x-ray-diffraction measurements reveal a 0.025% compression of the c axis accompanied by a 0.024% expansion of the a and b axes coinciding with the magnetic transition [44]. To conclusively identify this large spin-wave gap as fluctuation induced, we first determine whether these distortions could potentially account for its observed magnitude.

Since $S = 1/2$ pseudospins have both a spin and orbital contribution to their magnetic moment, they can couple more easily with lattice deformations of the appropriate symmetry [46]. Because of this coupling, the type-III ordering will necessarily generate structural deformations, which is consistent with the observed tetragonal distortion [44] and the reported anisotropic magnetization

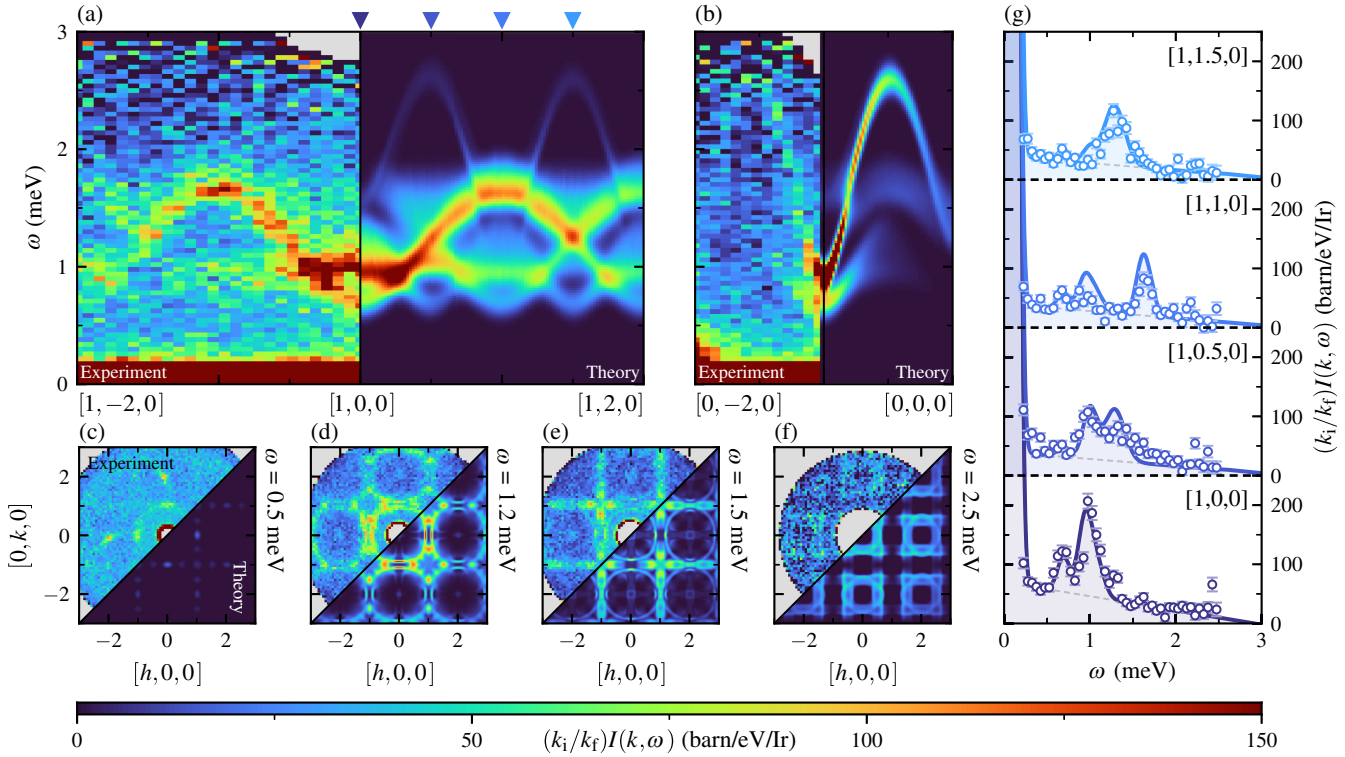

FIG. 3. Spin waves in the ordered phase of K_2IrCl_6. Measured (left) and calculated (right) energy-momentum slices along (a) $[1,k,0]$ and (b) $[0,k,0]$ integrated over $h \pm 0.15$ r.l.u. and $l \pm 0.15$ r.l.u. (c)–(f) Constant energy slices across the magnon spectra integrated over $\omega \pm 0.15$ meV. The measured spectrum is shown in the upper left, and the calculated spectrum is shown in the lower right. (g) Constant $\boldsymbol{Q}$ cuts at high-symmetry wave vectors indicated by colored arrows at the top of (a) and integrated over ± 0.1 r.l.u.. Data in panels (a)–(g) were collected at $T = 300$ mK, and error bars represent 1 standard deviation. Spectrum calculated at $O(1/S^2)$ using self-consistent nonlinear spin-wave theory for an fcc Heisenberg-Kitaev model with type-III magnetic order (domain averaged) using best-fit exchange parameters $J = 0.74$ meV and $K = 0.15$ meV.

density in K_2IrCl_6 [47]. Such magnetoelastic couplings will also give rise to spatially anisotropic exchange interactions D that can induce a magnon gap $\propto \sqrt{JD}$ [46], where J is the (dominant) Heisenberg exchange. We estimate the magnetic anisotropy from the measured tetragonal strain $\varepsilon \approx 2 \times 10^{-4}$ [44] and spin-lattice-coupling constant $\tilde{g} \simeq (t^2/U)3/2\lambda(J_H/U)$ where t, U, J_H, and λ are the hopping amplitude, Coulomb repulsion, Hund's coupling, and spin-orbit coupling, respectively [46]. Based on similar estimates in Sr_2IrO_4 [46], but with a nearest-neighbor exchange constant $J \sim t^2/U$ in K_2IrCl_6 that is a factor of approximately 100 smaller, we estimate $\tilde{g} \approx 0.25$ meV and thus, $D \sim \tilde{g}\varepsilon \approx 0.025$ μeV. This yields a distortion-induced gap of approximately 5 μeV—2-orders of magnitude too small to account for the observed 0.7-meV value [43]. As an additional check, we have carried out an LSWT calculation including all symmetry-allowed terms with only tetragonal symmetry [43]. This includes different exchanges within (J, K) and perpendicular to ($J_\perp, K_\perp$) the basal plane (perpendicular to the tetragonal axis). Fitting a tetragonal model that can account for the measured gap yields significant differences in the exchanges within the plane and in the perpendicular direction; the Heisenberg exchange yielding a modest $J_\perp/J = 1.29$, but a much larger $K_\perp/K = 1.93$ for the Kitaev exchange [43]. Given the smallness of the observed tetragonal distortion and our estimate of the magnetoelastic coupling, we find this level of spatial anisotropy in the exchanges implausible and rule it out as an explanation for the large spin-wave gap in our data.

B. Nonlinear spin-wave theory

Given that magnetic excitations in the ordered state of K_2IrCl_6 cannot be explained qualitatively by LSWT when cubic symmetry is maintained, we must then consider the effects of quantum fluctuations beyond LSWT. Including interactions between the spin waves can lift the pseudo-Goldstone modes, inducing a gap through quantum fluctuations [42,48]. To account for these fluctuation-induced gaps, we have computed the dynamical structure factor for the fcc Heisenberg-Kitaev (HK) model (as measured by inelastic neutron-scattering) about the type-III ordering using $O(1/S^2)$ self-consistent NLSWT [43]. As shown in Fig. 3, we find excellent quantitative agreement with our experimental data—including the large gap—using only nearest-neighbor Heisenberg exchange

$J = 0.74$ meV and Kitaev exchange $K = 0.15$ meV ($K/J = 0.2$). These exchange parameters are comparable to density functional theory predictions [36] and estimates from electron spin resonance measurements [38]. Neither the symmetric anisotropy Γ nor NNN interactions are required to describe the inelastic neutron data for K_2IrCl_6, suggesting they are small relative to J and K.

III. NODAL-LINE SPIN LIQUID

With the ordered phase understood, we now consider the paramagnetic nodal-line spin-liquid phase. In the absence of further-neighbor interactions, the fcc Heisenberg AFM supports a subextensive degeneracy and a finite-temperature nodal-line spin-liquid phase [Fig. 1]. Kitaev interactions in K_2IrCl_6 act to reduce the continuous symmetry of the Heisenberg model to a discrete one. Despite this symmetry reduction, we will show below that the subextensive degeneracy of the nodal-line spin liquid survives in the presence of significant anisotropic interactions and dictates some of the structure we have observed in the excitation spectrum.

A. Classical ground states from stacked states

To understand the qualitative features of the paramagnetic phase of K_2IrCl_6, we first revisit the classical phase diagram of the J-K-Γ model on the fcc lattice [43] using the Luttinger-Tisza method [49,50] that has been considered in previous works [36,40,51,52]. We find a rich phase diagram including multiple commensurate and incommensurate magnetic phases, as well as a broad region where $K > 0$ and $|\Gamma| < K/2$ that has a ground-state degeneracy along "spiral lines" with wave vectors $[q, 1, 0]$, $[0, q, 1]$, $[1, 0, q]$, and equivalents [43]. In the paramagnetic phase, these degeneracies imply the presence of spin correlations localized along these lines in reciprocal space (as would be found, e.g., in standard large-N treatment)—the key signature of the nodal-line spin liquid. Along these spiral lines, the Luttinger-Tisza energy is $E_0 = -2(J + K)S^2$ where S is the spin length, which provides a lower bound on the true classical ground-state energy.

A subextensive number of states that saturate this bound can be constructed by stacking Néel planes along the cubic directions, as illustrated in Fig. 2. Each plane has two possible choices for the Néel state that can be encoded by an Ising variable $\sigma_n^\mu = \pm 1$ with the index $\mu = x, y, z$ indicating the stacking direction. For each of these states, the contribution of the interplane couplings cancels for all J, K, and Γ, and only the plane perpendicular to the stacking direction contributes to the classical energy. For $K > 0$ and $|\Gamma| < K/2$ the intraplane energy is minimized by a Néel state (satisfying the Heisenberg part) with moment parallel to the stacking direction (satisfying the Kitaev part), with Γ dropping out.

For example, a type-I Néel state can be constructed by stacking Néel planes uniformly along the $\hat{\boldsymbol{x}}$ direction with the spins oriented along $\hat{\boldsymbol{x}}$, with the associated propagation vector (0, 0, 1), as shown in Fig. 2(a). The type-III state can be constructed from a $+1, +1, -1, -1$ stacking sequence corresponding to $(1/2, 1, 0)$ as shown in Fig. 2(b). Arbitrary stackings of the Néel planes along a fixed cubic direction give a large family of collinear stacked ground states. These stacked states are identical to those that make up the subextensive discrete degeneracy of the fcc Ising antiferromagnet [53]. Since there are two choices for the Néel state in each plane and three choices of stacking direction ($\hat{\boldsymbol{x}}, \hat{\boldsymbol{y}}$, or $\hat{\boldsymbol{z}}$), there are 3×2^{2L} collinear states where L is the number of cubic unit cells along the stacking direction. More explicitly, we can define three families of colinear stacked states as

$$\boldsymbol{S}_i^x = S(-1)^{n_1+n_2}\sigma^x_{n_2+n_3}\hat{\boldsymbol{x}}, \tag{2a}$$

$$\boldsymbol{S}_i^y = S(-1)^{n_2+n_3}\sigma^y_{n_3+n_1}\hat{\boldsymbol{y}}, \tag{2b}$$

$$\boldsymbol{S}_i^z = S(-1)^{n_3+n_1}\sigma^z_{n_1+n_2}\hat{\boldsymbol{z}}, \tag{2c}$$

where we have expressed the position $\boldsymbol{r}_i = n_1\boldsymbol{a}_1 + n_2\boldsymbol{a}_2 + n_3\boldsymbol{a}_3$ in terms of the primitive lattice vectors $\boldsymbol{a}_1$, $\boldsymbol{a}_2$, and $\boldsymbol{a}_3$.

This discrete subextensive degeneracy of collinear states does not exhaust the ground-state manifold. As these stacked states are collinear and can be oriented along perpendicular axes, linear combinations of these states can also be shown to be ground states. More explicitly, if we define

$$\boldsymbol{S}_i \equiv S[\alpha_x\boldsymbol{S}_i^x + \alpha_y\boldsymbol{S}_i^y + \alpha_z\boldsymbol{S}_i^z,], \tag{3}$$

where $\sum_\mu \alpha_\mu^2 = 1$, then we can see that these are normalized $|\boldsymbol{S}_i|^2 = 1$. The cross terms in the energy vanish for distinct stackings, yielding the same $-2(J + K)S^2$ energy. These mixed states thus establish a very large continuous manifold of ground states in the Heisenberg-Kitaev Hamiltonian relevant to K_2IrCl_6. For each discrete ground state, e.g., stacked along the $\hat{\boldsymbol{x}}$ direction, we can "rotate" it into two arbitrary ground states stacked in the $\hat{\boldsymbol{z}}$ and $\hat{\boldsymbol{y}}$ directions, producing a new (noncollinear) ground state.

This continuous manifold forms the basis of the nodal-line spin liquid and is a subset of the continuous manifold found in the Heisenberg limit when $J > 0$ and $K = \Gamma = 0$ [1,54]. In the Heisenberg limit, this manifold is considerably larger including, for example, the mixing of states stacked along the same direction, but with orthogonal moment directions. The presence of these continuously connected ground states affects the dynamics of K_2IrCl_6 within its ordered phase, implying that, at least at the LSWT level, the presence of gapless spin-wave modes along nodal lines in reciprocal space [43]. The absence of these low-lying excitations experimentally, and the necessity of going beyond the linear theory (Fig. 3), is thus a

strong signature of the significance of quantum effects in K_2IrCl_6.

B. Observation of the nodal-line spin liquid

With theoretical expectations established, we now examine the dynamics of K_2IrCl_6 in the paramagnetic phase. Figure 4 shows inelastic neutron-scattering data collected at $T = 6$ K. There are rods of intensity averaged over a broad energy window [Figs. 4(a) and 4(b)] that directly demonstrate two-dimensional correlations in K_2IrCl_6 well above the Néel transition $T_N = 3.1$ K. Such anisotropic, two-dimensional, correlations arising from an underlying isotropic, three-dimensional, magnetic Hamiltonian are the experimental signature of a nodal-line spin liquid.

The rods of intensity extend along equivalent $[1, q, 0]$ reciprocal-space directions characteristic of the set of coplanar spin spirals of the nodal-line spin liquid. Momentum-energy slices shown in Fig. 4(c) reveal a continuum of scattering extending from these rods, with intensity concentrated near $\boldsymbol{Q} = (1, 0, 0)$ momentum transfers and extending to 2 meV. There is no evidence for a buildup of critical intensity near the $\boldsymbol{Q} = (1, 0.5, 0)$ wave vector of the type-III magnetic ordering that appears below T_N. Instead, dynamic magnetic correlations are localized along lines in reciprocal space, establishing K_2IrCl_6 as a nodal-line spin-liquid state in this temperature regime.

We compare these correlations with expectations from the classical spin dynamics of the fcc HK model. As shown in Fig. 4(a), the low-energy-momentum-dependent correlations we observe are well captured by classical spin dynamics of our best-fit fcc HK model within its paramagnetic phase, further establishing the validity exchange parameters we have determined from the NLSWT in the ordered state of K_2IrCl_6. Although the classical calculation can reproduce much of the observed momentum-dependent scattering, there is a notable discrepancy for energy transfers above 1 meV where the data reveal an intensity maxima near $\boldsymbol{Q} = (1, 0, 0)$ not seen in the theoretical calculation [Figs. 4(b) and 4(d)]. This discrepancy reflects strong quantum fluctuations in K_2IrCl_6 that are not captured in the classical spin dynamics and redistributes magnetic fluctuations to higher energies.

Similar rods of scattering signifying emergent two-dimensional correlations have been observed in the pyrochlore XY ferromagnet $Yb_2Ti_2O_7$ [55–60]. While the emergence of correlations in reduced spatial dimension compared with the parent Hamiltonian is common between $Yb_2Ti_2O_7$ and the nodal-line spin liquid in K_2IrCl_6, there are essential differences between the respective origins of

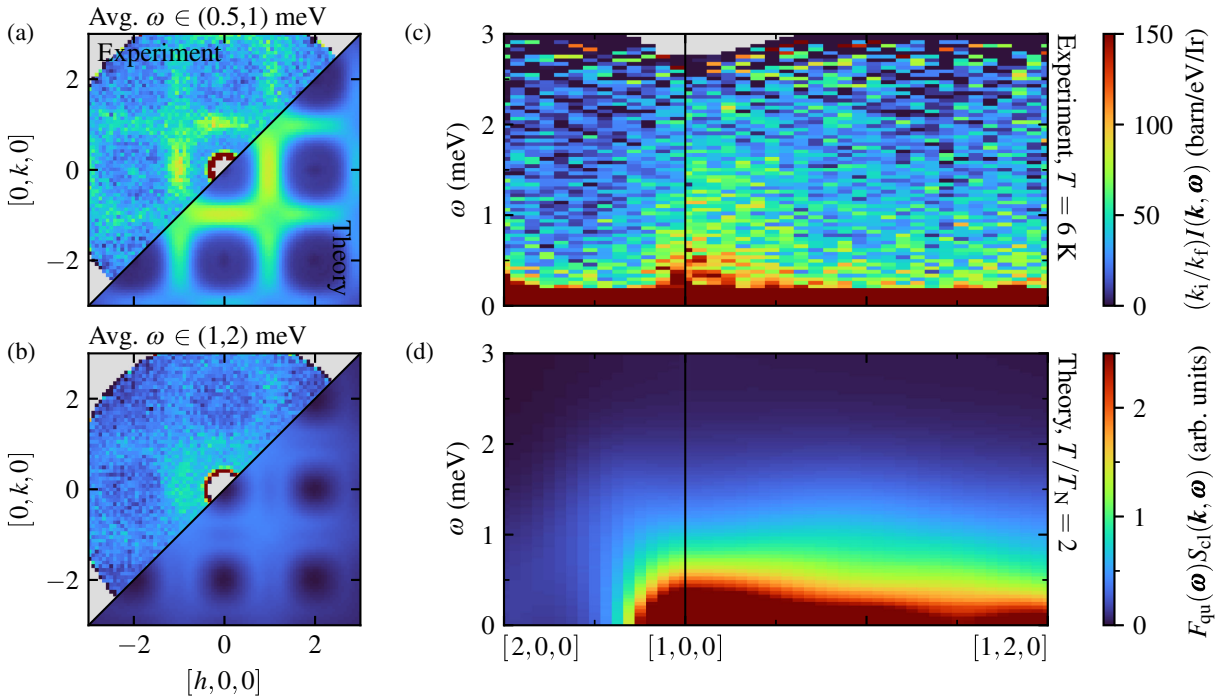

FIG. 4. Dynamic correlations of the nodal-line spin liquid. (a),(b) Constant energy neutron-scattering intensity at $T = 6$ K integrated over 0.5 to 1 meV in (a) and 1 to 2 meV in (b). Lower right of (a), and (b), shows the result from classical spin dynamics of our best-fit fcc Heisenberg-Kitaev model with exchange parameters $J = 0.74$ meV and $K = 0.15$ meV. (c) Momentum- and energy-resolved magnetic excitation spectra of the nodal-line spin liquid at $T = 6$ K. Momentum directions are integrated over ± 0.15 r.l.u.. (d) Classical spin dynamics at a temperature twice the model's ordering temperature computed as described in Ref. [43]. While these data are well above the Néel temperature, with $T/T_N \approx 2$, these temperatures are well below that characteristic Curie-Weiss energy scale with $T/\Theta_{CW} \approx 0.22$ where $\Theta_{CW} = (3J + K)/k_B \approx 27.4$ K.

the two. The XY Hamiltonian appropriate for $Yb_2Ti_2O_7$ has several competing phases that are very close in energy. Although there is a single, nondegenerate, ground state for a particular set of exchange interactions in the Hamiltonian, the actual exchange parameters in $Yb_2Ti_2O_7$ place it in close proximity to many of these phases. The two-dimensional rods of scattering are believed to arise from the proximity to both the ferromagnetic and antiferromagnetic phases [59,60]. This competition between two distinct phases that are proximal in energy is distinct from the emergent one-dimensional correlations of the nodal-line spin liquid in K_2IrCl_6, where the Hamiltonian describing the material has a (much larger) continuous subextensive degeneracy of ground states for a single set of exchange parameters.

Since the degeneracy of the nodal-line spin liquid scales subextensively, either fluctuations, small additional magnetic interactions, or both are expected to select a long-range ordered state as the temperature is lowered. Consistent with these expectations, K_2IrCl_6 undergoes a magnetic ordering transition into a type-III Néel state at $T_N = 3.1$ K. Our best-fit model for the magnetic excitation spectra, which contains only nearest-neighbor Heisenberg and Kitaev interactions, provides a quantitative description of the excitations in the ordered and nodal-line spin-liquid states of K_2IrCl_6. However, without further-neighbor interactions our model does not clearly predict a type-III ground state. Thermal fluctuations show a preference for type-I order, but even including fluctuations to $O(1/S^2)$ the energy difference between the type-I and -III states is expected to be incredibly small [48]. This close competition between type-I and -III states indicates the mechanism selecting type-III order in K_2IrCl_6 is delicate, and the ordering transition in K_2IrCl_6 deserves closer scrutiny.

IV. TYPE-I AND TYPE-III ORDER

Heat capacity measurements on our samples display a single sharp peak at 3.1 K, in agreement with the critical temperature extracted from the (1, 0.5, 0) magnetic order parameter [Figs. 5(a) and 5(b)]. However, a broader reciprocal-space survey on the same samples revealed additional weak magnetic Bragg reflections at $\boldsymbol{Q} = (1, 0, 0)$ corresponding to type-I order, with an onset temperature of $T_N^I = 3.4$ K, confirmed via neutron diffraction as shown in Fig. 5(b). The magnetic origin of (1, 0, 0) reflections was confirmed through energy- and polarization-dependent resonant x-ray diffraction that indicates an absence of any charge signal [Figs. 5(d)–5(f)]. The fine momentum-space resolution x-ray measurements also revealed that (0.5, 0, 5) magnetic Bragg peaks corresponding to type-III Néel order are resolution limited, while the (0, 0, 3) magnetic peak corresponding to type-I order has a finite correlation length of 877 Å. Although there is no heat capacity anomaly visible at T_N^I, we find substantial magnetic entropy extending beyond $T \sim 15$ K that is consistent

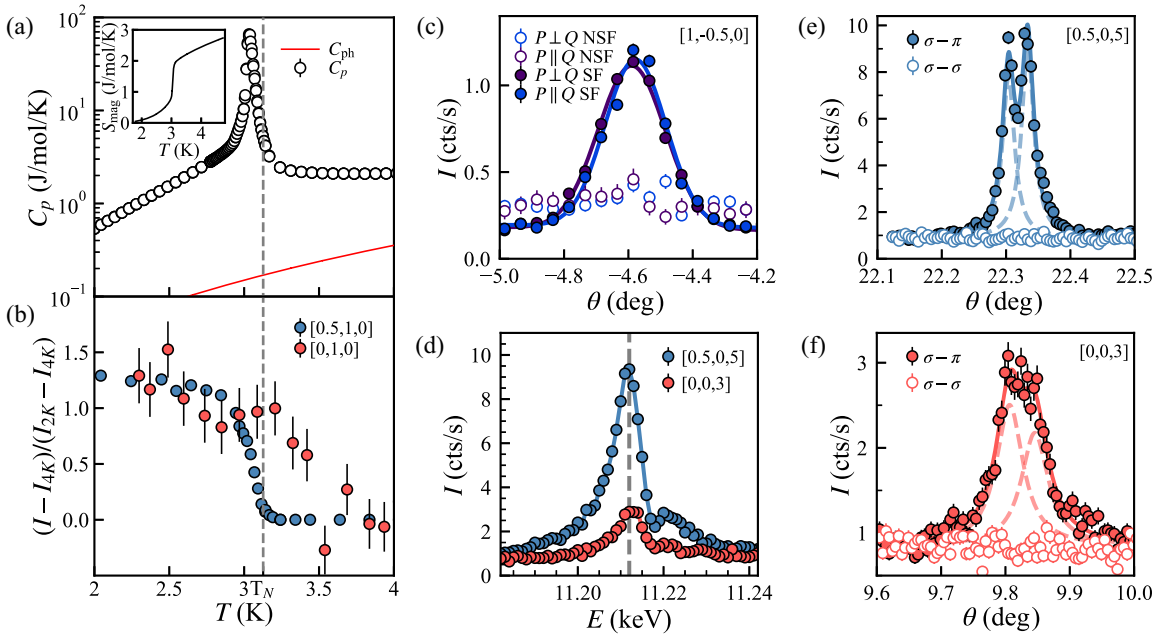

FIG. 5. Coexistence of type-I and -III collinear magnetic orders in K_2IrCl_6. (a) Measured zero-field specific heat C_p and estimated lattice contribution C_{ph}. (b) Temperature dependence of (0.5, 1, 0) (type-III) and (0, 1, 0) (type-I) intensities obtained from neutron diffraction. (c) Polarized neutron diffraction of a type-III peak at 1.5 K indicating the absence of a spin component along the [0, 0, 1] direction. (d) Energy-dependent elastic x-ray scattering demonstrating that both peaks arise from a magnetic resonance. Resonant x-ray rocking curves on (e) type-III and (f) type-I peaks at 2 K measured on the same crystal as for (a). Error bars in all panels represent 1 standard deviation.

with an extended regime of stability for the nodal-line spin liquid and the onset of short-range type-I order at 3.4 K.

A simultaneous appearance of (1, 0.5, 0) and (1, 0, 0) magnetic peaks is consistent with either a coexistence of collinear magnetic phases across multiple domains or a multi-Q order. Polarized neutron diffraction presented in Fig. 5(c) rules out the possibility of noncoplanar multi-Q states. The spin-flip neutron intensity of the $\boldsymbol{Q} = (1, -0.5, 0)$ Bragg reflection is sensitive to both in-plane and out-of-plane components of the magnetization for guide fields $\boldsymbol{P}$ parallel to $\boldsymbol{Q}$, and in-plane components of the magnetization, along $[1, 2, 0]$, for $\boldsymbol{P} \perp \boldsymbol{Q}$. While the non-spin-flip neutron intensity is only sensitive to out-of-plane components of the magnetization, along [0, 0, 1], when $\boldsymbol{P} \perp \boldsymbol{Q}$. We observed identical $(1, -0.5, 0)$ peak intensities for $\boldsymbol{P} \parallel \boldsymbol{Q}$ and $\boldsymbol{P} \perp \boldsymbol{Q}$ spin-flip channels, and no magnetic signal in the non-spin-flip component, ruling out any out-of-plane component, as expected for a collinear type-III Néel state [Fig. 5(c)]. We also find that the polarized diffraction from $\boldsymbol{Q} = (1, 0, 0)$ magnetic peaks is most consistent with a collinear arrangement of magnetic moments that are parallel to the [0, 0, 1] direction, expected for a type-I Néel state [43]. The linear polarization analysis presented here can rule out only noncoplanar ordering associated with each of the magnetic wave vectors. Neutron spherical polarimetry measurements are required to reveal the degree of collinearity and fully constrain the type-I and -III AFM ordering in K_2IrCl_6. Nevertheless, the polarized diffraction data support a coexistence of type-I and -III magnetic orders across different spatial regions of the sample. This is consistent with expectations from order by disorder, which strongly favor collinear single-Q states. From the integrated magnetic Bragg intensities, we extract a relative phase fraction $N_{\mathrm{I}}/N_{\mathrm{III}} \approx 11\%$. This phase fraction did not change between measurements on two different samples from different crystal growths indicating that the small fraction of the type-I phase is likely intrinsic and does not arise from quenched disorder in our samples.

The appearance of both type-I and -III orders near T_{N} in K_2IrCl_6 implicates weak and competing selection effects from fluctuations or further-neighbor exchange for these nearly degenerate states. To better understand the role of these selection mechanisms near T_{N}, we consider energetic selection via a NNN exchange J_2 in the classical model. When $J_2/J = 0$, we find that thermal order by disorder selects a type-I order for the fcc HK model [13,15,43]. A small $J_2/J \sim 0.02$ selects type-III order instead, onsetting at a nearly identical Néel temperature to the $J_2 = 0$ case [43]. Together, our data and modeling demonstrate that K_2IrCl_6 uniquely displays a competition between energetic and entropic mechanisms for order selection. Temperature-dependent neutron diffraction shown in Fig. 5(b) demonstrates that thermal fluctuations initially favor type-I order, but as the temperature is lowered and the influence of entropy diminishes, quantum fluctuations or weak further-neighbor interactions select type-III order. Such a competition between weak selection mechanisms for the magnetic order in K_2IrCl_6 is consistent with nearly negligible NNN interactions and underscores the dominant role played by quantum fluctuations in this material.

V. DISCUSSION

The conventional lore of frustrated quantum magnetism is that degenerate and competing ground states tend to suppress the tendency toward magnetic long-range order. In the quantum limit of $S = 1/2$, quantum fluctuations persist as $T \to 0$ and act to reduce the sublattice magnetization of any ordered state. Since the total moment $S(S+1)$ is conserved, this ordered moment reduction experimentally manifests as a transfer of neutron intensity from the magnetic Bragg peak (order parameter) to the excitations [61]. Thus, a sublattice magnetization that is reduced from the classical limit of gS_z is a direct indication of quantum fluctuations. K_2IrCl_6 presents an important counterpoint to these expectations, where despite a well-formed static Néel state and long-lived magnon excitations, higher-order (in $1/S$) corrections from quantum fluctuations are essential to describe the spectra on even a qualitative level.

The ordered moment reduction can be quantified through the energy distribution of magnetic neutron intensity. The momentum- and energy-integrated intensity gives the total moment of $g^2S(S+1)$, while the elastic intensity for a fully ordered moment is g^2S^2. Longitudinal fluctuations will tend to reduce the sublattice magnetization by a factor ΔS_z that can be quantified directly through the ratio of elastic to total integrated intensity $R = (S_z - \Delta S_z)^2/S(S+1)$. For K_2IrCl_6, we find $R \approx 0.31$, and a sublattice magnetization reduction of $\Delta S_z \approx 0.018$. This is consistent with both the ordered moment of $m = 0.85\ \mu_{\mathrm{B}}$ determined from our neutron-diffraction measurements saturating the classical sublattice magnetization of $gS_z = 0.89\ \mu_{\mathrm{B}}$, $g = 1.79$ [27,33,38], and with the small moment reduction predicted by NLSWT. Such a negligible reduction in sublattice magnetization for a highly frustrated magnet is surprising. For comparison, the zero-point moment reduction for a $S = 1/2$ Heisenberg antiferromagnet on a cubic lattice, where quantum fluctuations give negligible corrections, is $\Delta S \sim 0.078$ [62], demonstrating that by self-consistently generating a large spin-wave gap, quantum fluctuations are remarkably effective to stabilize the sublattice magnetization in K_2IrCl_6. This smallness of this correction makes clear that quantum fluctuations do not necessarily manifest in the ordered moment, but instead can appear in other characteristic features of the system, such as the excitation spectrum.

Above T_{N}, K_2IrCl_6 is a unique realization of a new classical spin liquid: the nodal-line spin liquid. This correlated paramagnet is similar to the spiral-spin liquid recently

observed in $MnSc_2S_4$ [3]. Both have a subextensive degeneracy and are susceptible to thermal order by disorder, but fluctuations in the nodal-line liquid are confined to one-dimensional lines instead of spiral surfaces. Despite this reduced degeneracy, the role of quantum fluctuations is significantly enhanced in K_2IrCl_6. Magnetic ordering in $MnSc_2S_4$ is controlled by further-neighbor, dipolar, and anisotropic exchange interactions, the excitation spectrum is fully described by LSWT [63,64], and there is no experimental support for an order-by-disorder transition [63–65]. This difference likely arises from the small $S = 1/2$ moments (Mn^{2+} is $S = 5/2$) and negligible dipolar interactions in K_2IrCl_6.

It is the scale of $1/S$ quantum fluctuations in K_2IrCl_6 that distinguishes it as an important frustrated magnet. These quantum fluctuations can be quantified by the relative size of the fluctuation-induced magnon gap compared to the bandwidth that exceeds 30% in K_2IrCl_6. For comparison, quantum order-by-disorder spin-wave gaps have been found in the garnet $Fe_2Ca_3(GeO_4)_3$ [66], the pyrochlore $Er_2Ti_2O_7$ [67–70], and the honeycomb lattice $CoTiO_3$ [71,72]. In all of these, the spin-wave gap-to-bandwidth ratio is less than 10% and nearly all details of the magnon spectra besides the fluctuation induced gaps are reproduced by linear spin-wave theory, while this fails qualitatively for K_2IrCl_6.

The scale of quantum fluctuations in K_2IrCl_6 is further reflected by the dynamics of the nodal-line spin-liquid phase that are only partially reproduced by a classical spin dynamics calculation. Such a departure from classical expectations is distinct from other correlated paramagnets. For example, even the excitation spectrum of the highly frustrated Heisenberg model on the pyrochlore lattice can be qualitatively captured by classical spin dynamics calculations renormalized by a classical-to-quantum correspondence factor [73]. Departures from renormalized classical spin dynamics calculations in the nodal-line spin liquid realized by K_2IrCl_6 calls for further work to understand the quantum-to-classical crossover in classical spin liquids.

ACKNOWLEDGMENTS

Work at Brown University was supported by the U.S. Department of Energy, Office of Basic Energy Sciences, under Grant No. DE-SC0021223. A portion of this research used resources at the Spallation Neutron Source and High Flux Isotope Reactor, the DOE Office of Science User Facilities operated by the Oak Ridge National Laboratory. Access to MACS was provided by the Center for High Resolution Neutron Scattering, a partnership between the National Institute of Standards and Technology and the National Science Foundation under Agreement No. DMR-2010792. This research used resources of the Advanced Photon Source, a U.S. Department of Energy Office of Science user facility operated for the DOE Office of Science by Argonne National Laboratory under Contract No. DE-AC02-06CH11357. Work at the University of Windsor was funded by the Natural Sciences and Engineering Research Council of Canada (Funding Reference No. RGPIN-2020-04970). We acknowledge the use of computational resources provided by Digital Research Alliance of Canada.

APPENDIX: METHODS

1. Sample synthesis and characterization

Commercially available powder of K_2IrCl_6 was obtained from Fisher Scientific. K_2IrCl_6 crystals were prepared by slow evaporation from a saturated solution of K_2IrCl_6 in dilute hydrochloric acid ($p\mathrm{H} \sim 3$). The evaporation process was controlled to maintain a temperature of 32 deg Celsius. Larger crystals were obtained by successive seeding of solution growths.

Specific heat and magnetization were measured in a Quantum Design Physical Properties Measurement System. Specific heat was measured upon warming in zero magnetic field after a zero-field cooling. Additional sample characterization is provided in Supplemental Material [43].

2. Neutron scattering

Inelastic neutron-scattering measurements were performed on a sample comprised of 11 coaligned crystals with total mass 0.3 g using the Cold Neutron Chopper Spectrometer (CNCS) at the Spallation Neutron Source at Oak Ridge National Laboratory (ORNL) and the MACS spectrometer [74] at the NIST Center for Neutron Research. The neutron momentum transfer is indexed using the Miller indices of the cubic unit cell, $(h,k,\ell) = (2\pi/a, 2\pi/a, 2\pi/a)$, where $a = 9.66$ Å, and all inelastic neutron-scattering data have been corrected for the energy-dependent neutron absorption from Ir [43].

On CNCS, we used an incident neutron energy of $E_i = 3.32$ meV in the high-flux configuration with a chopper frequency of 180 Hz to give an elastic line energy resolution of 0.17 meV (FWHM). A He cryostat and He^3 insert was used to cool the sample to a base temperature of $T = 0.3$ K. Data were collected for a 360° rotation of the sample with 1-deg step size. Measured neutron count rates were placed into absolute units of the neutron-scattering cross section using incoherent elastic scattering from the sample. The scale factor for conversion to absolute units was additionally cross-checked against the integrated intensity for (200) and (220) nuclear Bragg reflections. All data reduction and analysis were carried out using the MANTID software suite [75].

Measurements on MACS were conducted with the sample oriented in the (h,h,ℓ) scattering plane using a double-focusing configuration and fixed final energy of 3.7 meV with a BeO filter after the sample and no incident

beam filter. The data were corrected for contamination from high-order harmonics in the incident beam neutron monitor.

Unpolarized neutron-diffraction measurements were carried out on the HB-1A diffractometer of the High Flux Isotope Reactor (HFIR) at ORNL with collimations of 40'-40'-40'-80' and fixed incident energy $E_i = 14.5$ meV. Polarized neutron-diffraction measurements were carried out on the HB-1 triple-axis spectrometer of HFIR at ORNL with collimations of 48'-80'-60'-open and fixed incident energy $E_i = 13.5$ meV. Both experiments on HB-1A and HB-1 were conducted on the same single crystal with a mass of 42.5 mg aligned in the $(h, k, 0)$ scattering plane.

3. X-ray scattering

Resonant elastic x-ray-scattering measurements at the Ir L3 edge $E_i = 11.215$ keV were performed on Beamline 6-ID-B at the Advanced Photon Source. A Pilatus 100K detector with 487×195 pixels of 175×175 micron size was utilized for the measurement. Polarization analysis was performed using the (008) reflection of a pyrolytic graphite analyzer and the Cyberstar scintillator detector. A Joule-Thompson displex cryostat was used to reach a base temperature of 2 K. The resonant elastic x-ray scattering measurements were performed on the same sample used for heat capacity measurements.

4. Heisenberg-Kitaev model on the fcc lattice

We model the $j = 1/2$ doublets of the Ir^{4+} atoms as effective $S = 1/2$ spins $\boldsymbol{S}_i$ on an fcc lattice with an isotropic g factor. We consider a model with nearest-neighbor Heisenberg exchange and Kitaev exchanges [24,29,40]

$$\sum_{\langle ij\rangle_\gamma}\left[J\boldsymbol{S}_i\cdot\boldsymbol{S}_j + KS_i^\gamma S_j^\gamma\right], \tag{A1}$$

where we divide the bonds of the fcc lattice into three types: x, y, and z, depending on whether they lie in the yz, zx, or xy planes. When NNN interactions are included, we consider only a Heisenberg exchange $J_2\sum_{\langle\langle ij\rangle\rangle}\boldsymbol{S}_i\cdot\boldsymbol{S}_j$. Our best-fit parameters (as described in the main text) correspond to $J = 0.74$ meV and $K = 0.15$ meV.

5. Self-consistent nonlinear spin-wave theory

We consider a semiclassical expansion about the type-III ordered state, starting from the $S\to\infty$ limit. We use the Holstein-Primakoff representation [76] of the spin

$$\boldsymbol{S}_i \equiv \sqrt{S}\left[\left(1-\frac{n_{r\alpha}}{2S}\right)^{1/2} a_{r\alpha}\hat{\boldsymbol{e}}_{\alpha,-} + a_{r\alpha}^\dagger\left(1-\frac{n_{r\alpha}}{2S}\right)^{1/2}\hat{\boldsymbol{e}}_{\alpha,+}\right] + (S-n_{r\alpha})\hat{\boldsymbol{e}}_{\alpha,0}, \tag{A2}$$

where $n_{r\alpha}\equiv a_{r\alpha}^\dagger a_{r\alpha}$ and $i\equiv\boldsymbol{r},\alpha$ labels the unit cell and sublattice of a spin. For the collinear type-III orders a four-sublattice unit cell is sufficient for each of the domains. The vectors $\hat{\boldsymbol{e}}_{\alpha,\pm}\equiv(\hat{\boldsymbol{x}}_\alpha \pm i\hat{\boldsymbol{y}}_\alpha)/\sqrt{2}$ and $\hat{\boldsymbol{e}}_{\alpha,0}\equiv\hat{\boldsymbol{z}}_\alpha$ define a local frame with $\hat{\boldsymbol{z}}_\alpha$ being along the ordering directions of the type-III state. Expanding in powers of $1/S$ then yields a semiclassical expansion. Including terms up to $O(1)$ we find

$$H = NS(S+1)\epsilon_{\rm cl} + H_2 + H_4,$$

where the $O(S^2)$ part $\epsilon_{\rm cl}$ is the classical ground-state energy density, and we define the $O(S)$ and $O(1)$ parts in symmetrized form as

$$H_2 = \frac{1}{2}\sum_{\alpha\beta}\sum_{\boldsymbol{k}}\Big[A_{\boldsymbol{k}}^{\alpha\beta}a_{\boldsymbol{k}\alpha}^\dagger a_{\boldsymbol{k}\beta} + A_{-\boldsymbol{k}}^{\beta\alpha}a_{-\boldsymbol{k}\alpha}a_{-\boldsymbol{k}\beta}^\dagger + \left(B_{\boldsymbol{k}}^{\alpha\beta}a_{\boldsymbol{k}\alpha}^\dagger a_{-\boldsymbol{k}\beta}^\dagger + \bar{B}_{\boldsymbol{k}}^{\alpha\beta}a_{-\boldsymbol{k}\beta}a_{\boldsymbol{k}\alpha}\right)\Big], \tag{A3a}$$

$$H_4 = \frac{1}{N_c}\sum_{\alpha\beta\mu\nu}\sum_{\boldsymbol{k}\boldsymbol{k}'\boldsymbol{q}}\Big[\frac{1}{(2!)^2}V_{\boldsymbol{k}\boldsymbol{k}[\boldsymbol{q}]}^{\alpha\beta\mu\nu}a_{\boldsymbol{k}+\boldsymbol{q},\alpha}^\dagger a_{\boldsymbol{k}'-\boldsymbol{q},\beta}^\dagger a_{\boldsymbol{k}'\mu}a_{\boldsymbol{k}\nu} + \frac{1}{3!}\left(D_{\boldsymbol{k}\boldsymbol{k}'\boldsymbol{q}}^{\alpha\beta\mu\nu}a_{\boldsymbol{k}\alpha}^\dagger a_{\boldsymbol{k}'\beta}^\dagger a_{\boldsymbol{q}\mu}^\dagger a_{\boldsymbol{k}+\boldsymbol{k}'+\boldsymbol{q},\nu} + \text{H.c.}\right)\Big]. \tag{A3b}$$

In terms of the exchange matrices expressed in these local frames $\mathcal{J}_{\boldsymbol{\delta},\alpha\alpha'}^{\mu\mu'}\equiv\hat{\boldsymbol{e}}_{\alpha,\mu}^{\mathsf{T}}\boldsymbol{J}_{\boldsymbol{\delta},\alpha\alpha'}\hat{\boldsymbol{e}}_{\alpha',\mu'}$, the coefficients are

$$A_{\boldsymbol{k}}^{\alpha\beta} = S\left(\mathcal{J}_{\boldsymbol{k},\alpha\beta}^{+-} - \delta_{\alpha\beta}\sum_\mu\mathcal{J}_{\boldsymbol{0},\alpha\mu}^{00}\right), \tag{A4a}$$

$$B_{\boldsymbol{k}}^{\alpha\beta} = S\mathcal{J}_{\boldsymbol{k},\alpha\beta}^{++}, \tag{A4b}$$

$$V_{\boldsymbol{k}\boldsymbol{k}'[\boldsymbol{q}]}^{\alpha\beta\mu\nu} = \left(\delta_{\alpha\mu}\delta_{\beta\nu}\mathcal{J}_{\boldsymbol{k}-\boldsymbol{k}'+\boldsymbol{q},\alpha\beta}^{00}\delta_{\alpha\nu}\delta_{\beta\mu}\mathcal{J}_{\boldsymbol{q},\alpha\beta}^{00}\right) - \left(\delta_{\mu\nu}\delta_{\mu\beta}\mathcal{J}_{\boldsymbol{k}+\boldsymbol{q},\alpha\nu}^{+-} + \delta_{\alpha\beta}\delta_{\alpha\mu}\mathcal{J}_{\boldsymbol{k},\alpha\nu}^{+-}\right), \tag{A4c}$$

$$D_{\boldsymbol{k}\boldsymbol{k}'\boldsymbol{q}}^{\alpha\beta\mu\nu} = -\frac{3}{4}\left(\delta_{\alpha\mu}\delta_{\alpha\nu}\mathcal{J}_{\boldsymbol{k}',\beta\alpha}^{++} + \delta_{\mu\beta}\delta_{\nu\beta}\mathcal{J}_{\boldsymbol{k},\alpha\beta}^{++}\right), \tag{A4d}$$

where the interaction vertices have been left unsymmetrized for brevity.

At leading order in perturbation theory, these magnon interaction terms renormalize the LSWT spectrum, giving corrections to $\delta\boldsymbol{A}_{\boldsymbol{k}}$ and $\delta\boldsymbol{B}_{\boldsymbol{k}}$ to $\boldsymbol{A}_{\boldsymbol{k}}$ and $\boldsymbol{B}_{\boldsymbol{k}}$. We treat these corrections self-consistently by writing

$$\delta A^{\alpha\beta}_{\boldsymbol{k}} = \frac{1}{N_c}\sum_{\boldsymbol{q}\mu\nu}\left[V^{\alpha\mu\nu\beta}_{\boldsymbol{kq}[\boldsymbol{0}]}\langle a^\dagger_{\boldsymbol{q}\mu}a_{\boldsymbol{q}\nu}\rangle_{\mathrm{MF}} + \frac{1}{2}\left(D^{\alpha\mu\nu\beta}_{\boldsymbol{k},-\boldsymbol{q},\boldsymbol{q}}\langle a^\dagger_{-\boldsymbol{q}\mu}a^\dagger_{\boldsymbol{q}\nu}\rangle_{\mathrm{MF}} + \bar{D}^{\beta\mu\nu\alpha}_{\boldsymbol{k},\boldsymbol{q},-\boldsymbol{q}}\langle a_{\boldsymbol{q}\mu}a_{-\boldsymbol{q}\nu}\rangle_{\mathrm{MF}}\right)\right],$$

$$\delta B^{\alpha\beta}_{\boldsymbol{k}} = \frac{1}{N_c}\sum_{\boldsymbol{q}\mu\nu}\left[D^{\mu\alpha\beta\nu}_{\boldsymbol{q},\boldsymbol{k},-\boldsymbol{k}}\langle a^\dagger_{\boldsymbol{q}\mu}a_{\boldsymbol{q}\nu}\rangle_{\mathrm{MF}} + \frac{1}{2}V^{\alpha\beta\nu\mu}_{\boldsymbol{q},-\boldsymbol{q},[\boldsymbol{k}-\boldsymbol{q}]}\langle a_{\boldsymbol{q}\mu}a_{-\boldsymbol{q}\nu}\rangle_{\mathrm{MF}}\right].$$

where N_c is the number of unit cells, and the averages $\langle\cdots\rangle_{\mathrm{MF}}$ are with respect to the quadratic Hamiltonian $H_2 + \delta H_2$, where we have replaced $\boldsymbol{A}_{\boldsymbol{k}} \to \boldsymbol{A}_{\boldsymbol{k}} + \delta\boldsymbol{A}_{\boldsymbol{k}}$ and $\boldsymbol{B}_{\boldsymbol{k}} \to \boldsymbol{B}_{\boldsymbol{k}} + \delta\boldsymbol{B}_{\boldsymbol{k}}$. These equations are solved self-consistently (via iteration) to obtain an (effective) corrected quadratic Hamiltonian.

6. Calculation of inelastic neutron-scattering intensity

The inelastic neutron-scattering intensity is computed theoretically in terms of the spin-spin-correlation function

$$\mathcal{S}_{\mu\nu}(\boldsymbol{k},\omega) \equiv \frac{1}{2\pi N}\int dt e^{-i\omega t}\langle M^\mu_{-\boldsymbol{k}}M^\nu_{\boldsymbol{k}}(t)\rangle, \tag{A5}$$

where $\boldsymbol{M}_{\boldsymbol{k}} \equiv g\mu_{\mathrm{B}}\sum_i e^{-i\boldsymbol{k}\cdot\boldsymbol{r}_i}\boldsymbol{S}_i$ is the magnetization operator at wave vector $\boldsymbol{k}$, and N is the total number of spins. The observed intensity is given by

$$I(\boldsymbol{k},\omega) \propto F(k)^2\sum_{\mu\nu}\left(\delta_{\mu\nu} - \hat{k}_\mu\hat{k}_\nu\right)\mathcal{S}_{\mu\nu}(\boldsymbol{k},\omega), \tag{A6}$$

where $F(k)$ is the Ir^{4+} magnetic form factor.

Within linear spin-wave theory, the dynamical structure factor can be expressed in terms of the transverse-transverse part of the spin-spin correlation function. This remains true in our nonlinear spin-wave theory (up to an overall intensity renormalization), and $I(\boldsymbol{k},\omega)$ can be computed using the self-consistently determined $H_2 + \delta H_2$ as in LSWT. For more details, including the averaging needed to emulate the binning of the experimental data, we refer the reader to Supplemental Material [43].

7. Classical spin dynamics simulations

In the paramagnetic phase, we consider the fcc HK model with $J = 0.74$ meV and $K = 0.15$ meV in the classical limit where the spins are unit length vectors $|\boldsymbol{S}_i|^2 = 1$. The spins obey conventional Landau-Lifshitz dynamics

$$\frac{d\boldsymbol{S}_i}{dt} = -\boldsymbol{S}_i \times \frac{\partial H}{\partial \boldsymbol{S}_i}, \tag{A7}$$

where $-\partial H/\partial\boldsymbol{S}_i \equiv \boldsymbol{B}_i$ is the (local) exchange field due to the neighboring spins. The initial conditions $\boldsymbol{S}_i(0)$ are drawn from a thermal distribution at temperature T using Monte Carlo sampling. Once a sample of trajectories $\boldsymbol{S}_i(t)$ is obtained, the part of the dynamical structure factor relevant for inelastic neutron scattering is given by

$$\mathcal{S}_{\mathrm{cl}}(\boldsymbol{k},\omega) = \sum_{\mu\nu}\left(\delta_{\mu\nu} - \hat{k}_\mu\hat{k}_\nu\right)\langle\bar{S}^\mu_{\boldsymbol{k}}(\omega)S^\nu_{\boldsymbol{k}}(\omega)\rangle, \tag{A8}$$

where $\boldsymbol{S}_{\boldsymbol{k}}(\omega)$ is the Fourier transform of $\boldsymbol{S}_i(t)$ in both space and time. To account for K_2IrCl_6 being $S = 1/2$ we rescale frequencies by a factor of S, ensuring that in the low-temperature limit the classical and quantum spin-wave frequencies agree. To partially account for quantum effects we also multiply by an energy-dependent correction factor [59,73]

$$F_{\mathrm{qu}}(\omega) \equiv \beta\omega(1 + n_B(\omega)), \tag{A9}$$

where $n_B(\omega) = 1/(e^{\beta\omega} - 1)$ is the Bose distribution.

Thermal samples are generated using Monte Carlo with single-site heat bath [77] and over-relaxation [78] updates, annealing down from high temperature $O(10J)$ to the temperature of interest and then thermalizing for the same number of sweeps. For Fig. 4 in the paramagnetic phase only a small number of sweeps, typically $O(10^3)$, are necessary to reach equilibrium, and the system size used was $N = L^3$ with $L = 32$. For each initial state we solve the coupled nonlinear ordinary differential equations using an adaptive fourth-order Runge-Kutta method. At the temperatures of interest $O(10^2)$ samples are sufficient to reach convergence in both energy-resolved and energy-averaged quantities. The adaptive time stepping was performed with (absolute and relative) error tolerances of 10^{-8}.

Simulations used to establish the dependence of the ordering type and ordering temperature on J_2/J used a larger number of sweeps $O(10^5)$ on smaller system sizes with a conventional cell $N = 4L^3$ where $L = 8$, 10, 12, as well as parallel tempering to aid in reaching equilibrium. The phase transition temperature was inferred from the location of a sharp maximum in the heat capacity and the onset of a type-III order parameter.

[1] P. W. Anderson, *Generalizations of the Weiss molecular field theory of antiferromagnetism*, Phys. Rev. **79**, 705 (1950).

[2] D. Bergman, J. Alicea, E. Gull, S. Trebst, and L. Balents, *Order-by-disorder and spiral spin-liquid in frustrated diamond-lattice antiferromagnets*, Nat. Phys. **3**, 487 (2007).

[3] S. Gao, O. Zaharko, V. Tsurkan, Y. Su, J. S. White, G. S. Tucker, B. Roessli, F. Bourdarot, R. Sibille, D. Chernyshov, T. Fennell, A. Loidl, and C. Rüegg, *Spiral spin-liquid and*

the emergence of a vortex-like state in $MnSc_2S_4$, Nat. Phys. **13**, 157 (2017).
[4] J. Villain, *Insulating spin glasses*, Z. Phys. B **33**, 31 (1979).
[5] J. N. Reimers, A. J. Berlinsky, and A.-C. Shi, *Mean-field approach to magnetic ordering in highly frustrated pyrochlores*, Phys. Rev. B **43**, 865 (1991).
[6] R. Moessner and J. T. Chalker, *Properties of a classical spin liquid: The Heisenberg pyrochlore antiferromagnet*, Phys. Rev. Lett. **80**, 2929 (1998).
[7] C. L. Henley, *The "Coulomb phase" in frustrated systems*, Annu. Rev. Condens. Matter Phys. **1**, 179 (2010).
[8] K. W. Plumb, H. J. Changlani, A. Scheie, S. Zhang, J. W. Krizan, J. A. Rodriguez-Rivera, Y. Qiu, B. Winn, R. J. Cava, and C. L. Broholm, *Continuum of quantum fluctuations in a three dimensional* $S = 1$ *Heisenberg magnet*, Nat. Phys. **15**, 54 (2019).
[9] J. Villain, R. Bidaux, J.-P. Carton, and R. Conte, *Order as an effect of disorder*, J. Phys. (Les Ulis, Fr.) **41**, 1263 (1980).
[10] C. L. Henley, *Ordering by disorder: Ground-state selection in fcc vector antiferromagnets*, J. Appl. Phys. **61**, 3962 (1987).
[11] E. Rastelli and A. Tassi, *Order produced by quantum disorder in the Heisenberg rhombohedral antiferromagnet*, J. Phys. C **20**, L303 (1987).
[12] C. L. Henley, *Ordering due to disorder in a frustrated vector antiferromagnet*, Phys. Rev. Lett. **62**, 2056 (1989).
[13] M. V. Gvozdikova and M. E. Zhitomirsky, *A Monte Carlo study of the first-order transition in a Heisenberg FCC antiferromagnet*, JETP Lett. **81**, 236 (2005).
[14] M. E. Zhitomirsky, M. V. Gvozdikova, P. C. W. Holdsworth, and R. Moessner, *Quantum order by disorder and accidental soft mode in* $Er_2Ti_2O_7$, Phys. Rev. Lett. **109**, 077204 (2012).
[15] R. Schick, T. Ziman, and M. E. Zhitomirsky, *Quantum versus thermal fluctuations in the fcc antiferromagnet: Alternative routes to order by disorder*, Phys. Rev. B **102**, 220405(R) (2020).
[16] A. Danielian, *Ground state of an Ising face-centered cubic lattice*, Phys. Rev. Lett. **6**, 670 (1961).
[17] T. Yildirim, A. B. Harris, and E. F. Shender, *Frustration and quantum fluctuations in Heisenberg fcc antiferromagnets*, Phys. Rev. B **58**, 3144 (1998).
[18] C. A. Bailey and P. L. Smith, *Specific heats of ammonium, potassium, and sodium chloroiridates*, Phys. Rev. **114**, 1010 (1959).
[19] D. T. Haar and M. E. Lines, *A molecular-field theory of anisotropic ferromagnetica*, Philos. Trans. R. Soc. A **254**, 521 (1962).
[20] D. T. Haar and M. E. Lines, *A spin-wave theory of anisotropic antiferromagnetica*, Philos. Trans. R. Soc. A **255**, 1 (1962), 73109.
[21] M. E. Lines, *Antiferromagnetism in the face-centred cubic lattice by a spin-wave method*, Proc. R. Soc. A **271**, 105 (1963).
[22] R. Tahir-Kheli, H. Callen, and H. Jarrett, *Magnetic ordering in cubic crystals with first and second neighbor exchange*, J. Phys. Chem. Solids **27**, 23 (1966).
[23] M. Matsuura, Y. Endoh, H. Hiraka, K. Yamada, A. S. Mishchenko, N. Nagaosa, and I. V. Solovyev, *Classical and quantum spin dynamics in the fcc antiferromagnet* NiS_2 *with frustration*, Phys. Rev. B **68**, 094409 (2003).
[24] A. A. Aczel, A. M. Cook, T. J. Williams, S. Calder, A. D. Christianson, G.-X. Cao, D. Mandrus, Y.-B. Kim, and A. Paramekanti, *Highly anisotropic exchange interactions of* $j_{\mathrm{eff}} = \frac{1}{2}$ *iridium moments on the fcc lattice in* La_2BIrO_6 *(*B = Mg, *Zn)*, Phys. Rev. B **93**, 214426 (2016).
[25] P. Balla, Y. Iqbal, and K. Penc, *Degenerate manifolds, helimagnets, and multi-Q chiral phases in the classical Heisenberg antiferromagnet on the face-centered-cubic lattice*, Phys. Rev. Res. **2**, 043278 (2020).
[26] J. Owen, *Exchange interactions in antiferromagnetic salts of iridium*, J. Phys. Radium **20**, 138 (1959).
[27] J. H. E. Griffiths, J. Owen, J. G. Park, M. F. Partridge, and B. Bleaney, *Exchange interactions in antiferromagnetic salts of iridium. I. Paramagnetic resonance experiments*, Proc. R. Soc. London Ser. A **250**, 84 (1959).
[28] A. H. Cooke, R. Lazenby, F. R. McKim, J. Owen, and W. P. Wolf, *Exchange interactions in antiferromagnetic salts of iridium II. Magnetic susceptibility measurements*, Proc. R. Soc. London Ser. A **250**, 97 (1959).
[29] Judd Brian Raymond, *Exchange interactions in antiferromagnetic salts of iridium III. Theory of the interaction*, Proc. R. Soc. London Ser. A **250**, 110 (1959).
[30] E. A. Harris and J. Owen, *The magnetic properties of three exchange coupled iridium ions*, Proc. R. Soc. London Ser. A **289**, 122 (1965).
[31] M. T. Hutchings and C. G. Windsor, *The magnetic structure of* K_2IrCl_6, Proc. Phys. Soc. **91**, 928 (1967).
[32] V. Minkiewicz, G. Shirane, B. Frazer, R. Wheeler, and P. Dorain, *Neutron diffraction study of magnetic ordering in* K_2IrCl_6, K_2ReBr_6 *and* K_2ReCl_6, J. Phys. Chem. Solids **29**, 881 (1968).
[33] J. W. Lynn, G. Shirane, and M. Blume, *Covalency effects in the magnetic form factor of Ir in* K_2IrCl_6, Phys. Rev. Lett. **37**, 154 (1976).
[34] H. W. Willemsen, R. L. Armstrong, and P. P. M. Meincke, *Thermal expansion measurements near the antiferromagnetic phase transitions in* K_2ReCl_6 *and* K_2IrCl_6, J. Low Temp. Phys. **26**, 299 (1977).
[35] D. Moses, M. Sutton, R. L. Armstrong, and P. P. M. Meincke, *Specific heat measurements at low temperatures in* K_2MCl_6 *antifluorite crystals*, J. Low Temp. Phys. **36**, 587 (1979).
[36] N. Khan, D. Prishchenko, Y. Skourski, V. G. Mazurenko, and A. A. Tsirlin, *Cubic symmetry and magnetic frustration on the fcc spin lattice in* K_2IrCl_6, Phys. Rev. B **99**, 144425 (2019).
[37] D. Reig-i-Plessis, T. A. Johnson, K. Lu, Q. Chen, J. P. C. Ruff, M. H. Upton, T. J. Williams, S. Calder, H. D. Zhou, J. P. Clancy, A. A. Aczel, and G. J. MacDougall, *Structural, electronic, and magnetic properties of nearly ideal* $J_{\mathrm{eff}} = \frac{1}{2}$ *iridium halides*, Phys. Rev. Mater. **4**, 124407 (2020).
[38] L. Bhaskaran, A. N. Ponomaryov, J. Wosnitza, N. Khan, A. A. Tsirlin, M. E. Zhitomirsky, and S. A. Zvyagin, *Antiferromagnetic resonance in the cubic iridium hexahalides* $(NH_4)_2IrCl_6$ *and* K_2IrCl_6, Phys. Rev. B **104**, 184404 (2021).
[39] G. Jackeli and G. Khaliullin, *Mott insulators in the strong spin-orbit coupling limit: From Heisenberg to a quantum*

compass and Kitaev models, Phys. Rev. Lett. **102**, 017205 (2009).

[40] A. M. Cook, S. Matern, C. Hickey, A. A. Aczel, and A. Paramekanti, *Spin-orbit coupled* $J_{\text{eff}} = \frac{1}{2}$ *iridium moments on the geometrically frustrated fcc lattice*, Phys. Rev. B **92**, 020417(R) (2015).

[41] At nearest-neighbor level, this also includes bond-dependent Γ exchanges [24,29,40] of the form

$$\Gamma \sum_{\langle ij\rangle_{\alpha\beta(\gamma)}} (-1)^{\sigma_{ij}^{\alpha\beta}} (S_i^\alpha S_j^\beta + S_i^\alpha S_j^\beta),$$

where the sign is determined by the bond direction $\boldsymbol{d}_{ij} \equiv \boldsymbol{r}_j - \boldsymbol{r}_i$ as $\sigma_{ij}^{\alpha\beta} \equiv \text{sgn}(d_{ij}^\alpha d_{ij}^\beta)$.

[42] J. G. Rau, P. A. McClarty, and R. Moessner, *Pseudo-Goldstone gaps and order-by-quantum disorder in frustrated magnets*, Phys. Rev. Lett. **121**, 237201 (2018).

[43] See Supplemental Material at http://link.aps.org/supplemental/10.1103/PhysRevX.15.021021 for further details of the sample characterization, additional supporting neutron-scattering data, details of classical spin dynamics and nonlinear spin-wave theory, and considerations of the effects of a tetragonal distortion.

[44] Q. Wang, A. De La Torre, W. Tian, A. A. Aczel, J. C. Neuefeind, M. M. Everett, Y. Feng, M. H. Upton, J.-H. Kim, P. J. Ryan, J.-W. Kim, and K. W. Plumb (to be published).

[45] S. Lee, B. H. Kim, M.-J. Seong, and K.-Y. Choi, *Noncubic local distortions and spin-orbit excitons in* K_2IrCl_6, Phys. Rev. B **105**, 184433 (2022).

[46] H. Liu and G. Khaliullin, *Pseudo-Jahn-Teller effect and magnetoelastic coupling in spin-orbit Mott insulators*, Phys. Rev. Lett. **122**, 057203 (2019).

[47] J. Lynn, H. Patterson, G. Shirane, and R. Wheeler, *Soft rotary mode and structural phase transitions in* K_2ReCl_6, Solid State Commun. **27**, 859 (1978).

[48] R. Schick, O. Götze, T. Ziman, R. Zinke, J. Richter, and M. E. Zhitomirsky, *Ground-state selection by magnon interactions in a fcc antiferromagnet*, Phys. Rev. B **106**, 094431 (2022).

[49] J. M. Luttinger and L. Tisza, *Theory of dipole interaction in crystals*, Phys. Rev. **70**, 954 (1946).

[50] D. B. Litvin, *The Luttinger-Tisza method*, Physica (Utrecht) **77**, 205 (1974).

[51] I. Kimchi and A. Vishwanath, *Kitaev-Heisenberg models for iridates on the triangular, hyperkagome, kagome, fcc, and pyrochlore lattices*, Phys. Rev. B **89**, 014414 (2014).

[52] S.-S. Diop, G. Jackeli, and L. Savary, *Anisotropic exchange and noncollinear antiferromagnets on a noncentrosymmetric fcc half-Heusler structure*, Phys. Rev. B **105**, 144431 (2022).

[53] J. M. Luttinger, *A note on the ground state in antiferromagnetics*, Phys. Rev. **81**, 1015 (1951).

[54] S. Alexander and P. Pincus, *Phase transitions of some fully frustrated models*, J. Phys. A **13**, 263 (1980).

[55] K. A. Ross, J. P. C. Ruff, C. P. Adams, J. S. Gardner, H. A. Dabkowska, Y. Qiu, J. R. D. Copley, and B. D. Gaulin, *Two-dimensional kagome correlations and field induced order in the ferromagnetic xy pyrochlore* $Yb_2Ti_2O_7$, Phys. Rev. Lett. **103**, 227202 (2009).

[56] K. A. Ross, L. R. Yaraskavitch, M. Laver, J. S. Gardner, J. A. Quilliam, S. Meng, J. B. Kycia, D. K. Singh, T. Proffen, H. A. Dabkowska, and B. D. Gaulin, *Dimensional evolution of spin correlations in the magnetic pyrochlore* $Yb_2Ti_2O_7$, Phys. Rev. B **84**, 174442 (2011).

[57] C. R. C. Buhariwalla, Q. Ma, L. DeBeer-Schmitt, K. G. S. Xie, D. Pomaranski, J. Gaudet, T. J. Munsie, H. A. Dabkowska, J. B. Kycia, and B. D. Gaulin, *Long-wavelength correlations in ferromagnetic titanate pyrochlores as revealed by small-angle neutron scattering*, Phys. Rev. B **97**, 224401 (2018).

[58] A. Scheie, J. Kindervater, S. Zhang, H. J. Changlani, G. Sala, G. Ehlers, A. Heinemann, G. S. Tucker, S. M. Koohpayeh, and C. Broholm, *Multiphase magnetism in* $Yb_2Ti_2O_7$, Proc. Natl. Acad. Sci. U.S.A. **117**, 27245 (2020).

[59] A. Scheie, O. Benton, M. Taillefumier, L. D. C. Jaubert, G. Sala, N. Jalarvo, S. M. Koohpayeh, and N. Shannon, *Dynamical scaling as a signature of multiple phase competition in* $Yb_2Ti_2O_7$, Phys. Rev. Lett. **129**, 217202 (2022).

[60] H. Yan, O. Benton, L. Jaubert, and N. Shannon, *Theory of multiple-phase competition in pyrochlore magnets with anisotropic exchange with application to* $Yb_2Ti_2O_7$, $Er_2Ti_2O_7$, *and* $Er_2Sn_2O_7$, Phys. Rev. B **95**, 094422 (2017).

[61] S.-H. Lee, C. Broholm, M. F. Collins, L. Heller, A. P. Ramirez, Ch. Kloc, E. Bucher, R. W. Erwin, and N. Lacevic, *Less than 50% sublattice polarization in an insulating* $S = 3/2$ *kagomé antiferromagnet at* $T \approx 0$, Phys. Rev. B **56**, 8091 (1997).

[62] P. W. Anderson, *An approximate quantum theory of the antiferromagnetic ground state*, Phys. Rev. **86**, 694 (1952).

[63] A. Krimmel, M. Mücksch, V. Tsurkan, M. M. Koza, H. Mutka, C. Ritter, D. V. Sheptyakov, S. Horn, and A. Loidl, *Magnetic ordering and spin excitations in the frustrated magnet* $MnSc_2S_4$, Phys. Rev. B **73**, 014413 (2006).

[64] S. Gao, H. D. Rosales, F. A. Gómez Albarracín, V. Tsurkan, G. Kaur, T. Fennell, P. Steffens, M. Boehm, P. Čermák, A. Schneidewind, E. Ressouche, D. C. Cabra, C. Rüegg, and O. Zaharko, *Fractional antiferromagnetic skyrmion lattice induced by anisotropic couplings*, Nature (London) **586**, 37 (2020).

[65] S. Gao *et al.*, *Manifolds of magnetic ordered states and excitations in the almost Heisenberg pyrochlore antiferromagnet* $MgCr_2O_4$, Phys. Rev. B **97**, 134430 (2018).

[66] Th. Brueckel, B. Dorner, A. G. Gukasov, V. P. Plakhty, W. Prandl, E. F. Shender, and O. P. Smirnow, *Dynamical interaction of antiferromagnetic subsystems: A neutron scattering study of the spinwave spectrum of the garnet* $Fe_2Ca_3(GeO_4)_3$, Z. Phys. B **72**, 477 (1988).

[67] J. D. M. Champion, M. J. Harris, P. C. W. Holdsworth, A. S. Wills, G. Balakrishnan, S. T. Bramwell, E. Č Čižmár, T. Fennell, J. S. Gardner, J. Lago, D. F. McMorrow, M. Orendáč, A. Orendáčová, D. McK. Paul, R. I. Smith, M. T. F. Telling, and A. Wildes, $Er_2Ti_2O_7$*: Evidence of quantum order by disorder in a frustrated antiferromagnet*, Phys. Rev. B **68**, 020401(R) (2003).

[68] J. P. C. Ruff, J. P. Clancy, A. Bourque, M. A. White, M. Ramazanoglu, J. S. Gardner, Y. Qiu, J. R. D. Copley, M. B. Johnson, H. A. Dabkowska, and B. D. Gaulin, *Spin waves*

and quantum criticality in the frustrated XY pyrochlore antiferromagnet $Er_2Ti_2O_7$, Phys. Rev. Lett. **101**, 147205 (2008).

[69] L. Savary, K. A. Ross, B. D. Gaulin, J. P. C. Ruff, and L. Balents, *Order by quantum disorder in* $Er_2Ti_2O_7$, Phys. Rev. Lett. **109**, 167201 (2012).

[70] K. A. Ross, Y. Qiu, J. R. D. Copley, H. A. Dabkowska, and B. D. Gaulin, *Order by disorder spin wave gap in the XY pyrochlore magnet* $Er_2Ti_2O_7$, Phys. Rev. Lett. **112**, 057201 (2014).

[71] B. Yuan, I. Khait, G.-J. Shu, F. C. Chou, M. B. Stone, J. P. Clancy, A. Paramekanti, and Y.-J. Kim, *Dirac magnons in a honeycomb lattice quantum XY magnet* $CoTiO_3$, Phys. Rev. X **10**, 011062 (2020).

[72] M. Elliot, P. A. McClarty, D. Prabhakaran, R. D. Johnson, H. C. Walker, P. Manuel, and R. Coldea, *Order-by-disorder from bond-dependent exchange and intensity signature of nodal quasiparticles in a honeycomb cobaltate*, Nat. Commun. **12**, 3936 (2021).

[73] S. Zhang, H. J. Changlani, K. W. Plumb, O. Tchernyshyov, and R. Moessner, *Dynamical structure factor of the three-dimensional quantum spin liquid candidate* $NaCaNi_2 \times F_7$, Phys. Rev. Lett. **122**, 167203 (2019).

[74] J. A. Rodriguez, D. M. Adler, P. C. Brand, C. Broholm, J. C. Cook, C. Brocker, R. Hammond, Z. Huang, P. Hundertmark, J. W. Lynn, N. C. Maliszewskyj, J. Moyer, J. Orndorff, D. Pierce, T. D. Pike, G. Scharfstein, S. A. Smee, and R. Vilaseca, *MACS—A new high intensity cold neutron spectrometer at NIST*, Meas. Sci. Technol. **19**, 034023 (2008).

[75] O. Arnold *et al.*, *MANTID—Data analysis and visualization package for neutron scattering and* μSR *experiments*, Nucl. Instrum. Methods Phys. Res., Sect. A **764**, 156 (2014).

[76] T. Holstein and H. Primakoff, *Field dependence of the intrinsic domain magnetization of a ferromagnet*, Phys. Rev. **58**, 1098 (1940).

[77] Y. Miyatake, M. Yamamoto, JJ. Kim, M. Toyonaga, and O. Nagai, *On the implementation of the "heat bath" algorithms for Monte Carlo simulations of classical Heisenberg spin systems*, J. Phys. C **19**, 2539 (1986).

[78] M. Creutz, *Overrelaxation and Monte Carlo simulation*, Phys. Rev. D **36**, 515 (1987).